

Pseudopotential Bethe-Salpeter calculations for shallow-core x-ray absorption near-edge structures: excitonic effects in α - Al_2O_3

M. Laura Urquiza,^{1,2} Matteo Gatti,^{1,2,3} and Francesco Sottile^{1,2}

¹*LSI, CNRS, CEA/DRF/IRAMIS, École Polytechnique, Institut Polytechnique de Paris, F-91120 Palaiseau, France*

²*European Theoretical Spectroscopy Facility (ETSF)*

³*Synchrotron SOLEIL, L'Orme des Merisiers, Saint-Aubin, BP 48, F-91192 Gif-sur-Yvette, France*

(Dated: January 12, 2023)

We present an ab initio description of optical and X-ray absorption spectroscopies, in a unified formalism based on the pseudopotential plane-wave method at the level of the Bethe-Salpeter Equation (BSE) within Green's functions theory. We show that norm-conserving pseudopotentials are very reliable and accurate not only for valence, but also for semi-core electron absorption spectra. In order to validate our approach, we compare BSE results with two codes: **EXC**, based on pseudopotentials, and **Exciting**, an all-electron full-potential code. We take corundum α - Al_2O_3 as an example, a prototypical system that presents strong electron-hole interaction in both valence and core electron excitations. We analyze the optical, as well as the L_1 and $L_{2,3}$ edges, in detail in terms of anisotropy, crystal local fields, interference and excitonic effects. We conclude with a thorough inspection of the origin and localization of bright and dark excitons.

I. INTRODUCTION

X-ray absorption spectroscopy (XAS) and optical absorption are complementary techniques to determine materials properties. In optical absorption, valence electrons are excited into unoccupied conduction states across the band gap (or the Fermi energy in metals). Their excitations determine the color (or the transparency) of materials and are crucial to many materials properties and functionalities, spanning from optoelectronics to solar energy conversion and storage. In XAS, promoted to unoccupied conduction bands are instead core electrons, tightly bound to the nuclei. X-ray absorption near-edge structures (XANES), also known as near-edge X-ray absorption fine structure (NEXAFS), being element specific, is a probe of the atomic environment, giving structural and chemical information¹. In the simplest independent-particle picture, XANES spectra are proportional to the unoccupied density of states, projected on the absorbing atom and the angular momentum component that is selected by dipole selection rules, whereas optical spectra can be interpreted on the basis of the joint density of states of valence and conduction bands. In both spectroscopies, the interaction between the excited electron and the hole left behind can strongly alter this independent-particle picture. Indeed, the electron-hole attraction can give rise to excitons, i.e bound electron-hole pairs, leading to a transfer of spectral weight to lower energies in the spectra, including the formation of sharp peaks at their onset.

Given the importance of XANES spectroscopy, several theoretical methods have been developed to interpret the measured spectra in solids, taking care of core-hole effects at different levels of approximation². The most efficient approaches are, on one side, multiple scattering methods³⁻⁸, and, on the other side, multiplet models⁹⁻¹¹. While the former usually neglect the electronic interactions, the latter are often semi-empirical (i.e., not entirely

parameter-free) and generally neglect solid-state effects, being a many-body solution of finite-cluster models. Since the excitations of the core electrons are localised at the absorbing atoms, delta-self-consistent-field (Δ SCF) methods can be also employed, nowadays usually within first-principles density-functional theory¹²⁻²⁰. The core-excited atom is treated as an impurity in a supercell approach, and the presence of the core hole is taken into account in different ways, from the $Z+1$ approximation^{21,22} (the absorbing atom is assumed to have one additional nuclear charge), to the half core-hole approximation^{23,24} (also known as Slater's transition-state method) or the full core-hole approximation (the electron removed from the core is put at lowest conduction band, or ionized). Alternatively, XANES excitation spectra can be directly obtained within linear-response theory^{25,26}, which is the standard approach for valence excitations and optical spectra as well²⁷. In this case, two possible options are time-dependent density-functional theory²⁸⁻³⁰ (TDDFT) and the Bethe-Salpeter equation³¹⁻³⁵ (BSE) of Green's function theory^{36,37}. Since TDDFT lacks of efficient approximations for describing accurately excitonic effects in solids³⁸, the BSE, even though computationally more expensive, is usually more reliable²⁷. In the present work, the solution of the BSE will therefore be also our preferred choice to simulate valence and shallow-core excitation spectra within the same formalism.

In the simulation of core excitation spectra, the intuitive technique to represent the single-particle wave functions are all-electron methods. They explicitly deal with core electrons in extended materials by partitioning the space into interstitial and muffin-tin (MT) regions, where wave functions are described differently according to their localisation degree³⁹⁻⁴². Instead, methods that are based on plane-wave expansions cannot deal explicitly with the quickly oscillatory behavior of core electrons, tightly localised near the nuclei, which are instead generally taken into account effectively through the design of suitable pseudopotentials⁴³. Plane-wave methods

are computationally cheaper and new theoretical developments are easier to implement in plane-waves computer codes. Moreover, the separation between core electrons, kept frozen, and valence electrons, treated explicitly, is often not rigid. Between valence and deep core electrons, there are often also shallow core (or semicore) electrons, which in the pseudopotential framework can be in principle also treated as valence electrons, although at a price of higher computational cost. However, in all the cases, the pseudopotential formalism also introduces an important approximation, requiring a pseudization of the valence wave functions near the nuclei that make them smoother and node free. In the recent past, much work has been devoted to assess pseudopotential calculations for excited-state properties with respect to all-electron methods, notably for self-energy calculations of quasiparticle band structure energies^{44–51}. In the present work, we directly address the question of the validity of the pseudopotential approximation for XANES spectra of shallow-core edges (i.e., for electron binding energies smaller than ~ 180 eV), investigating the limits of use of pseudo wave functions for shallow core states in many-body BSE calculations. It is clear that the description of deep core levels will be always out of reach for plane-wave basis methods. However, the high plane-wave cutoff required by semicore states can be now alleviated by the new generation of ultrasoft norm-conserving pseudopotentials⁵². Besides the promised lower computational cost for shallower core levels, an advantage of pseudopotential plane-wave calculations with respect to all-electron methods is that they do not make any hypothesis concerning the localisation of the core hole inside the muffin tin⁵³.

In particular, here we investigate the effects of the electron-hole interactions on the optical absorption and shallow-core XANES spectra of alumina. $\alpha\text{-Al}_2\text{O}_3$ is a wide-gap insulator, with many possible applications as a structural ceramic (e.g. as a replacement to SiO_2 gate oxide technology) and optical material (also thanks to the high-damage threshold for UV laser applications), and a prototypical system to investigate core-hole effects in XANES spectroscopy^{12,54–59}.

The article is organised as follows. After a short description of the employed methodology in Sec. II, comprising a review of the theoretical background (Sec. II A) and a summary of the computational details (Sec. II B), Sec. III presents the results of the calculations together with their analysis. In Sec. III B pseudopotential calculations are assessed with respect to all-electron benchmarks for both optical and Al $L_{2,3}$ XANES spectra, while Sec. III C contains a discussion on the issue of the core-hole localisation in the muffin tin for the Al L_1 XANES spectrum. Sec. III D compares the calculated spectra with available experiments and analyses the effects of the electron-hole interactions on the spectra. Finally, Sec. IV draws the conclusions summarizing the results of the work.

II. METHODOLOGY

A. Theoretical background

In the framework of Green's function theory³⁶, the Bethe-Salpeter equation (BSE) yields the density response function from the solution of a Dyson-like equation for the two-particle correlation function⁶⁰. In the GW approximation (GWA) to the self-energy⁶¹, with a statically screened Coulomb interaction W , the BSE takes the form of an excitonic Hamiltonian²⁷ in the basis $|v\mathbf{c}\mathbf{k}\rangle$ of transitions between occupied $v\mathbf{k}$ and unoccupied bands $\mathbf{c}\mathbf{k}$ (i.e., uncorrelated electron-hole pairs):

$$\langle v\mathbf{c}\mathbf{k}|H_{\text{exc}}|v'\mathbf{c}'\mathbf{k}'\rangle = E_{v\mathbf{c}\mathbf{k}}\delta_{vv'}\delta_{cc'}\delta_{\mathbf{k}\mathbf{k}'} + \langle v\mathbf{c}\mathbf{k}|\bar{v}_c - W|v'\mathbf{c}'\mathbf{k}'\rangle. \quad (1)$$

Here $E_{v\mathbf{c}\mathbf{k}} = E_{\mathbf{c}\mathbf{k}} - E_{v\mathbf{k}}$ are the interband transition energies calculated in the GWA, while \bar{v}_c is the Coulomb interaction without its macroscopic component (i.e., the component $\mathbf{G} = 0$ in reciprocal space). The statically screened Coulomb interaction $W = \epsilon^{-1}v_c$ is usually calculated adopting the random-phase approximation (RPA) for the inverse dielectric function ϵ^{-1} .

The GWA-BSE is nowadays the state-of-the-art approach for the simulation, interpretation and prediction of optical spectra in solids^{36,37,62–64}, and is more and more used also for the simulation of core-level excitation spectra^{2,65–81}. A great advantage of theory with respect to experiments is the possibility to separately suppress (or activate) the various interactions at play in the materials, which allows one to single out their specific effect on the spectra and the materials properties. By setting to zero the two electron-hole interactions, \bar{v}_c and $-W$, the excitonic Hamiltonian (1) reduces to a diagonal matrix and corresponds to the independent-particle approximation (IPA). By switching on the electron-hole exchange interaction \bar{v}_c in Eq. (1), one retrieves the RPA. With respect to the IPA, the RPA includes the so-called crystal local field effects. They are related to the inhomogeneous charge response of materials through the induced microscopic Hartree potentials counteracting the external perturbations. Finally, by also switching on the electron-hole direct interaction $-W$, the full BSE (1) describes excitonic effects, which are due to the electron-hole attraction.⁸² The electron-hole interactions contributing to the off-diagonal matrix elements of the BSE (1) give rise to a mixing of the independent-particle transitions, which is formally obtained from the solution of the eigenvalue equation for the excitonic hamiltonian: $H_{\text{exc}}A_\lambda = E_\lambda A_\lambda$.

The absorption spectra, expressed both in the optical and XANES regimes by the imaginary part of the macroscopic dielectric function, $\text{Im}\epsilon_M(\omega)$, in the long wavelength limit $\mathbf{q} \rightarrow 0$, in the so-called Tamm-Dancoff approximation can be directly written in terms of eigenvectors A_λ and eigenvalues E_λ of the BSE Hamiltonian

(1) as:

$$\text{Im}\epsilon_M(\omega) = \lim_{\mathbf{q} \rightarrow 0} \frac{8\pi^2}{\Omega q^2} \sum_{\lambda} \left| \sum_{v\mathbf{ck}} A_{\lambda}^{v\mathbf{ck}} \tilde{\rho}_{v\mathbf{ck}}(\mathbf{q}) \right|^2 \delta(\omega - E_{\lambda}), \quad (2)$$

where Ω is the crystal volume, and $\tilde{\rho}_{v\mathbf{ck}}(\mathbf{q}) = \int \varphi_{v\mathbf{k}-\mathbf{q}}^*(\mathbf{r}) e^{-i\mathbf{q}\cdot\mathbf{r}} \varphi_{v\mathbf{k}}(\mathbf{r}) d\mathbf{r}$ are the independent-particle oscillator strengths. Here the single-particle orbitals φ_i are usually Kohn-Sham orbitals. If the exciton energy E_{λ} is smaller than the smallest independent-particle transition energy $E_{v\mathbf{ck}}$, the exciton λ is said to be bound: the difference between $E_{v\mathbf{ck}}$ and E_{λ} is its binding energy.

The contribution of each exciton λ to the spectrum can be analysed by introducing the cumulative function:

$$S_{\lambda}(\omega) = \lim_{\mathbf{q} \rightarrow 0} \frac{8\pi}{\Omega q^2} \left| \sum_{v\mathbf{ck}}^{E_{v\mathbf{ck}} < \omega} A_{\lambda}^{v\mathbf{ck}} \tilde{\rho}_{v\mathbf{ck}}(\mathbf{q}) \right|^2. \quad (3)$$

Since the eigenvectors A_{λ} and the oscillator strengths $\tilde{\rho}(\mathbf{q})$ are both complex quantities, the cumulative function (3) is not a monotonic function of ω . The limit $S_{\lambda}(\omega \rightarrow \infty)$ is the oscillator strength of the exciton λ in the absorption spectrum. If it is negligibly small, the exciton is said to be dark, otherwise it is called a bright exciton, for it contributes to the spectrum. Even in the $\mathbf{q} \rightarrow 0$, the oscillator strengths $\tilde{\rho}(\mathbf{q})$ depends on the direction of \mathbf{q} , so each exciton λ can at the same time be a bright exciton in one polarization direction and dark in another.

Finally, the investigation of the electron-hole correlation function for each exciton λ ,

$$\Psi_{\lambda}(\mathbf{r}_h, \mathbf{r}_e) = \sum_{v\mathbf{ck}} A_{\lambda}^{v\mathbf{ck}} \phi_{v\mathbf{k}}^*(\mathbf{r}_h) \phi_{v\mathbf{k}}(\mathbf{r}_e), \quad (4)$$

gives information about the localisation in real space of the electron-hole pair, which results from the electron-hole attraction. Assuming that the hole is in a specific position $\mathbf{r}_h = \mathbf{r}_h^0$, one can visualize the corresponding density distribution of the electron $|\Psi_{\lambda}(\mathbf{r}_h^0, \mathbf{r}_e)|^2$.

B. Computational details

We have performed calculations using both a pseudopotential (PP) plane-wave method and a full-potential all-electron (AE) linearized augmented plane-wave method. AE calculations have been done in particular to assess the validity of PP calculations for the core-level excitations (see Sec. IIIB). The converged BSE absorption spectra and their analysis (see Sec. IIID) have been then obtained in the PP framework. In the pseudopotential case, we have used the **Abinit** code⁸³ for the ground-state and screening calculations, and the **EXC** code⁸⁴ for the BSE calculations. In the all-electron case, we have used the **Exciting** code⁸⁵ for obtaining all the benchmark results.

The Kohn-Sham ground-state calculations have been performed within the local density approximation⁸⁶ (LDA).

We have employed norm-conserving Troullier-Martins⁸⁷ (TM) and optimized norm-conserving Vanderbilt^{52,88} (ONCVPSP) pseudopotentials. In particular, for the absorption spectra a special TM pseudopotential⁸⁹ treating also Al 2s and 2p states as valence electrons has been used. Calculation with the ONCVPSP pseudopotential converged with 42 Hartree cutoff of the plane-wave expansion, while the hard TM pseudopotential required 320 Hartree.

The statically screened Coulomb interaction W has been obtained (within the RPA) with the ONCVPSP pseudopotential (without Al 2s and 2p core levels), including 100 bands, and with a cutoff of 8 and 14.7 Hartree for the Kohn-Sham wave functions for the optical and shallow-core excitations, respectively. The size of the screening matrix in the plane-wave basis was 6 Hartree for the optical and 8 Hartree for the core spectrum. We have verified that, contrary to calculations of the screened interaction for other materials like silicon⁵⁰ or simple metals⁹⁰⁻⁹², the effect of core polarization is negligible in α -Al₂O₃.

In the all-electron results, the ground-state calculations were performed using a plane wave cutoff, $R_{\text{MT}}|\mathbf{G} + \mathbf{k}|_{\text{max}}$, of 18 Hartree and muffin-tin (MT) spheres R_{MT} of $2a_0$ and $1.45a_0$ for aluminum and oxygen, respectively. The RPA screening was obtained with 100 conduction bands and a cutoff in the matrix size of 5 Hartree (maintaining the same cutoff of the ground state for the plane waves).

The GW band structure has been approximated within a scissor correction model. The LDA conduction bands have been rigidly shifted upwards by 2.64 eV, which corresponds to the band gap correction obtained within the perturbative G_0W_0 scheme by Marinopoulos and Grüning⁹³.

The BSE calculations for the absorption spectra have been performed with shifted \mathbf{k} -point grids (i.e., not containing high-symmetry \mathbf{k} points), which allowed for a quicker convergence of the spectra⁶³. The optical absorption spectrum converged with a $10 \times 10 \times 10$ \mathbf{k} -point grid, while the XANES spectra at the Al L_{2,3} and L₁ edges converged with a $8 \times 8 \times 8$ \mathbf{k} -point grid. The exciton analysis and plot have been instead done with a smaller Γ -centered $4 \times 4 \times 4$ \mathbf{k} -point grid.

The BSE spectra for the optical spectrum or the XANES spectra at the Al L_{2,3} and L₁ edges had a different convergence rate with respect to the number of empty bands considered in the BSE hamiltonian. Fig. 1 shows their convergence study (carried out here with a reduced number of \mathbf{k} points in a Γ -centered $2 \times 2 \times 2$ \mathbf{k} -point grid). While the optical spectrum (left panel) quickly converges with the number of empty bands, the XANES spectra (middle and right panels) require many more empty bands, also to converge the lowest energy peak. In the converged spectra, obtained with many more \mathbf{k}

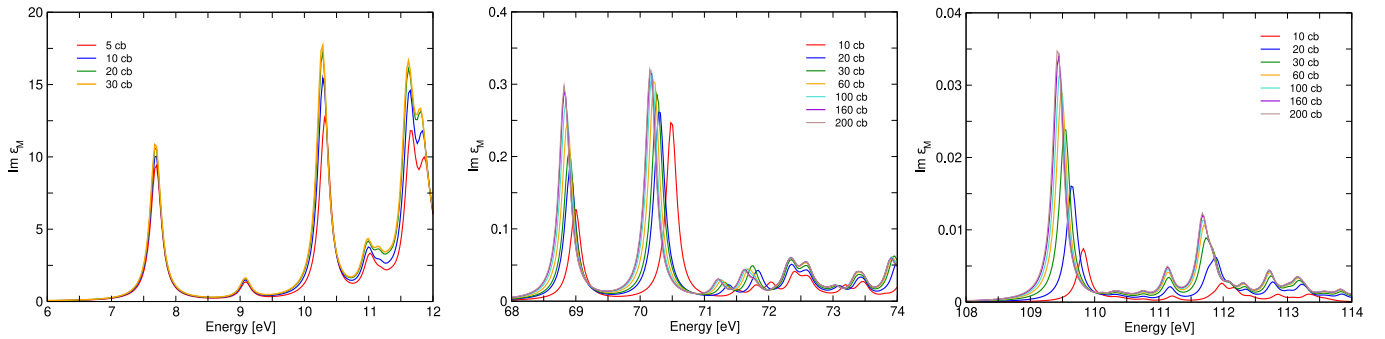


FIG. 1: Convergence of BSE absorption spectra with the number of unoccupied conduction bands (cb). (Left) Optical spectrum. (Middle) XANES at $L_{2,3}$ edge. (Right) XANES at L_1 edge.

points, this slow convergence is partially attenuated by the fact that the spectra become smoother. The optical absorption spectra have been thus obtained with 12 valence bands and 12 unoccupied bands. The XANES spectra at the $L_{2,3}$ and L_1 edges included all the corresponding core levels together with 30 unoccupied bands. A 0.1 eV Lorentzian broadening has been applied to the spectra.

In the all-electron BSE calculations, we considered the same parameters used in the calculation of the screening: 9 Hartree for the wavefunction cutoff and 5 Hartree to describe the electron-hole terms. In the pseudopotential BSE calculations, we have used a 30 Hartree cutoff for the Kohn-Sham wavefunctions expansion and 7.3 Hartree for the plane-wave representation of the electron-hole interactions. We note that, as usual (see e.g.⁹⁴), the plane-wave cutoffs for the BSE matrix elements can be significantly reduced with respect to the high cutoff needed for the ground-state calculation. Therefore, even for pseudopotential BSE calculations of shallow-core excitations, the limiting factor remains the large size of the BSE hamiltonian (1) in extended systems, which is given by the number of electron-hole transitions (i.e., the number of occupied bands \times the number of unoccupied bands \times the number of \mathbf{k} points in the full Brillouin zone).

III. RESULTS

A. Crystal and electronic structure of $\alpha\text{-Al}_2\text{O}_3$

The crystal structure of corundum $\alpha\text{-Al}_2\text{O}_3$ is trigonal (see Fig. 2). In the primitive rhombohedral unit cell (space group $R\bar{3}c$, number 167) there are two formula units. The corundum structure can also be viewed as a hexagonal cell containing six formula units with alternate layers of Al and O atoms in planes perpendicular to the hexagonal c_H axis. In the $\alpha\text{-Al}_2\text{O}_3$ structure all Al atoms occupy octahedral sites coordinated with 6 O atoms, which form two equilateral triangles located respectively slightly above and below each Al atom along the c_H direction.

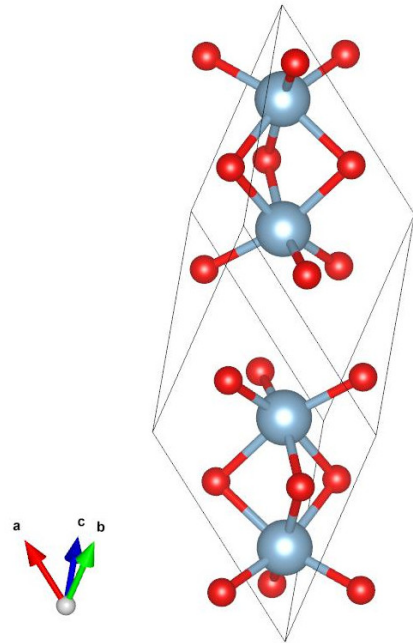


FIG. 2: Primitive rhombohedral unit cell of the crystal structure of $\alpha\text{-Al}_2\text{O}_3$. Red and grey balls represent O and Al atoms, respectively. The Al atoms are aligned along the cartesian z axis, which is the vertical direction in the figure, while the O atoms belong to the xy planes perpendicular to it.

We adopted the experimental lattice parameters from Ref.⁹⁵: $a_H = b_H = 4.7589 \text{ \AA}$ and $c_H = 12.991 \text{ \AA}$ in the hexagonal unit cell, which corresponds to $a_R = 5.128 \text{ \AA}$ and $\alpha = 55.287^\circ$ in the rhombohedral primitive cell. In the reference frame used in the simulations, the hexagonal c_H axis is aligned along the cartesian z axis, which is the vertical direction in Fig. 2.

The left panel of Fig. 3 shows the Kohn-Sham LDA band structure along a high symmetry path in the first Brillouin zone, together with the projected density of states on the O (middle panel) and Al (right panel) atoms. $\alpha\text{-Al}_2\text{O}_3$ has a direct bandgap at the Γ point,

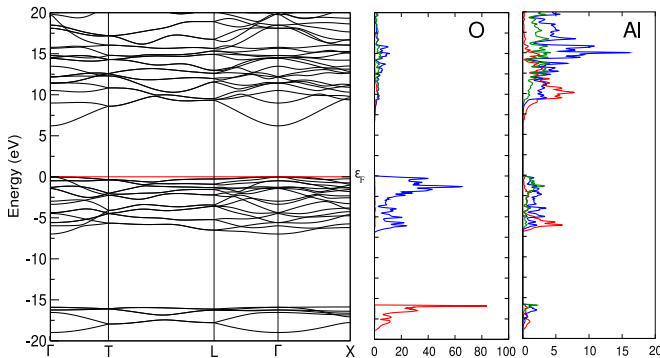


FIG. 3: (Left) LDA Kohn-Sham band structure of α - Al_2O_3 . The top of the valence band has been set to zero. Density of states projected on (middle) O and (right) Al atoms, resolved in the angular components: s (red), p (blue) and d (green).

which amounts to 6.21 eV in the LDA. This value is in very good agreement with the result of Ref. 96 obtained with the same experimental lattice parameters. Calculations^{93,96–98} that adopt a crystal structure optimised within the LDA, rather than the experimental one, instead obtain larger band gaps. In particular, the difference with respect to Ref. 93 is 0.51 eV. We refer to Ref. 98 for a detailed analysis of the dependence on the band gap on the lattice parameters. As usual, the Kohn-Sham band gap underestimates the experimental fundamental gap, estimated to be 9.57 eV from temperature-dependent vacuum ultraviolet (VUV) spectroscopy⁵⁵ and 9.6 eV from conductivity measurements⁹⁹.

The 6 bands located between -19 eV and -15.9 eV are the O $2s$ states, while the upper 18 valence bands, starting at ~ -7 eV, are mostly due to O $2p$ states, partially hybridised with Al states. The valence bands are quite flat along the entire path. The bottom conduction band consists of Al $3s$ hybridised with O $3s$ at the Γ point and also with O $2p$ elsewhere, showing a strong dispersion around the Γ point. The higher conduction bands have mainly Al $3p$ and $3d$ character, also hybridised with O states. This overview of the electronic properties confirms the intermediate covalent-ionic nature of the chemical bond in α - Al_2O_3 .

Finally, the Al $2p$ and $2s$ core levels (not shown in Fig. 3) in LDA are located 61.7 eV and 99.4 eV below the top valence, which, as usual, largely underestimates the experimental values¹⁰⁰ of 70.7 eV and 115.6 eV, respectively. The calculations do not include the spin-orbit coupling, so the $2p_{1/2}$ and $2p_{3/2}$ levels are not split. In all cases, we have verified that pseudopotential and all-electron calculations give the same band structures and core-level energies.

B. All-electron benchmark

One of the main goals of this work is to demonstrate that shallow core spectra can be calculated with high accuracy using the pseudopotential (PP) approximation. The importance of this objective is underlined by the many works in the same spirit^{101–104}. However, at variance with previous works that concern tests on ground-state properties, mostly related to total-energy calculations, here we aim at a much more stringent test, which involves occupied (both valence and semi-core) and unoccupied states. The latter could be in particular affected by the presence of ghost states¹⁰⁵, which could jeopardize completely the excitation spectrum, while leaving unaffected a total energy calculation. Therefore, in order to validate the optical and core spectra calculated with PPs, we benchmark the results with full-potential all-electron (AE) calculations, considered as a gold-standard method for solving DFT in extended systems^{85,106}. In order to perform this comparison properly, for both optical and $L_{2,3}$ edge absorption spectra the same choice of valence electrons is made in the two calculations, and the number of plane wave was converged consistently in the two cases.

The valence and $L_{2,3}$ spectra obtained at different levels of approximations, IPA, RPA and BSE, are shown in the top and bottom panels of Fig. 4, respectively. We can make several observations: i) The results of the left panels of Fig.4 show that the pseudopotential approximation reproduces the all-electron spectra with excellent accuracy within the IPA. ii) For the RPA spectrum (central panels) we find a similar result. This is in part related to the fact that local fields effects are not important in the energy ranges considered. iii) Finally, also the BSE calculations with the two approaches are in very good agreement. Recent comparisons⁸¹ between all-electron and projected augmented wave method approaches, for instance, present much bigger discrepancies than our results appearing in the right panels of Fig.4. The origin of this residual difference lies in the different treatment between the two codes of the integrable singularity of the diagonal matrix elements of W in (1), calculated in reciprocal space, when $\mathbf{k} - \mathbf{k}' = \mathbf{q} = 0$ and the reciprocal-lattice vectors are $\mathbf{G} = \mathbf{G}' = 0$. We note that the different treatment of this singularity was already mentioned also recently in a comparison among different GW codes¹⁰⁷. This singularity is, in fact, eliminated, by evaluating the integral

$$-\frac{4\pi}{\Omega} \epsilon_{\mathbf{G}=0, \mathbf{G}'=0}^{-1}(\mathbf{q} \rightarrow 0) \frac{1}{(2\pi)^3} \int_{\Omega_{\mathbf{q}=0}} d\mathbf{q} \frac{1}{q^2},$$

where $\Omega_{\mathbf{q}=0} = \Omega_{BZ}/N_k$. In order to carry out, numerically or analytically, the integral, one has to define the shape for the little volume $\Omega_{\mathbf{q}=0}$ around the origin of the Brillouin zone and, in anisotropic materials, choose the $\mathbf{q} \rightarrow 0$ direction in order to evaluate the inverse dielectric function $\epsilon^{-1}(\mathbf{q} \rightarrow 0)$. The details about how this integral is performed are in Ref.¹⁰⁸ and Refs.^{109,110}, for EXC

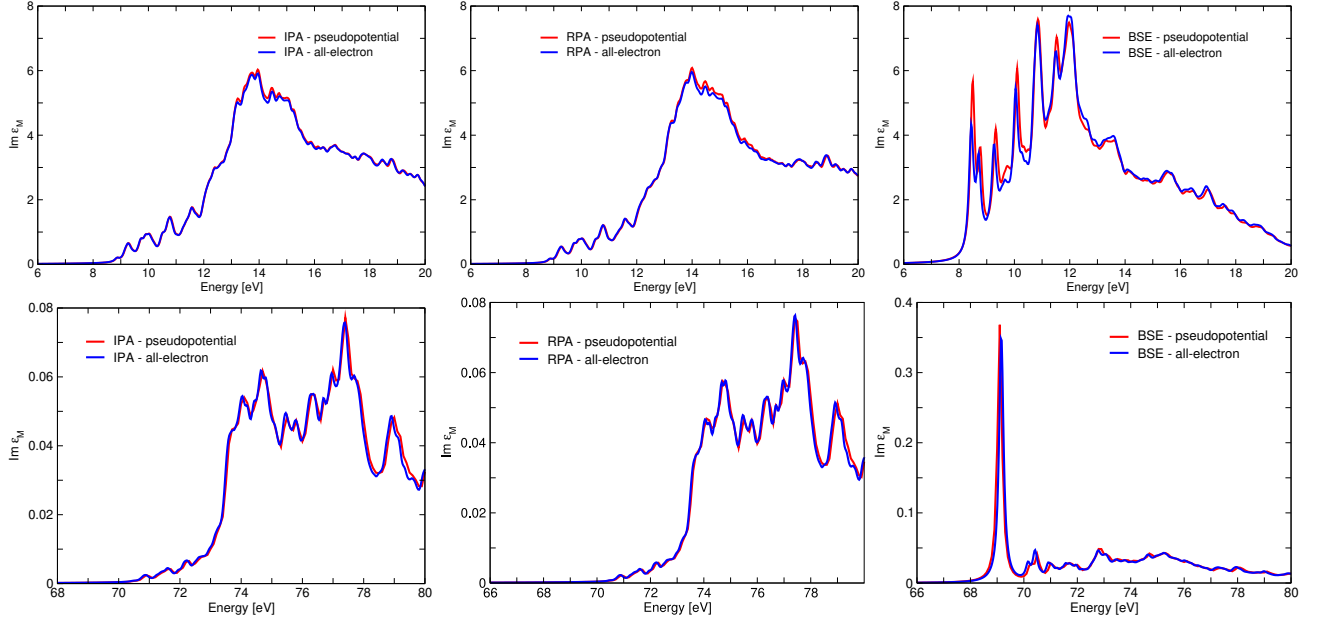


FIG. 4: Comparison of absorption spectra calculated with pseudopotential (red lines) and all-electron (blue lines) methods, using an unshifted $8 \times 8 \times 8$ \mathbf{k} -point grid, (left panels) in the independent particle approximation (IPA), (middle panels) in the random-phase approximation (RPA), (right panels) from the full Bethe-Salpeter equation (BSE). (Upper panels) Optical spectra (with 12 valence bands and 20 conduction bands). (Bottom panels) XANES spectra at Al L_{23} edge (with 12 core levels and 12 conduction bands).

and **Exciting**, respectively. If we exclude this singular contribution, the two BSE results become superposed, as in the IPA case. In addition, this contribution vanishes (more or less rapidly according to the kind of exciton¹¹¹) in the convergency with \mathbf{k} points. Fig. 5 indeed shows that the differences in the spectra obtained with the two codes tend to vanish with increasing number of \mathbf{k} points. Most importantly for the scope of the present work, we find that the differences between the PP and AE codes remain always of the same order of magnitude for both valence and shallow-core spectra. Therefore, in summary, we can safely conclude that the benchmarks with the all-electron approach show that pseudopotential calculations for optical and XANES spectroscopies (with semi-core states) are reliable and accurate.

C. Interference effects at the L_1 edge

The comparison between all-electron and pseudopotential approximation is more delicate for the L_1 edge, since the electrons are treated differently in the two codes. While **Exciting** includes the 2s states of Al inside the muffin-tin, in **EXC** they are considered as valence and treated with plane-waves.

One of the limitations of the linearized augmented-plane-wave (LAPW) method is that it could give a wrong description of semicore states when they are considered inside the muffin-tin (MT) sphere, but they overlap significantly with valence electrons or are too extended to be

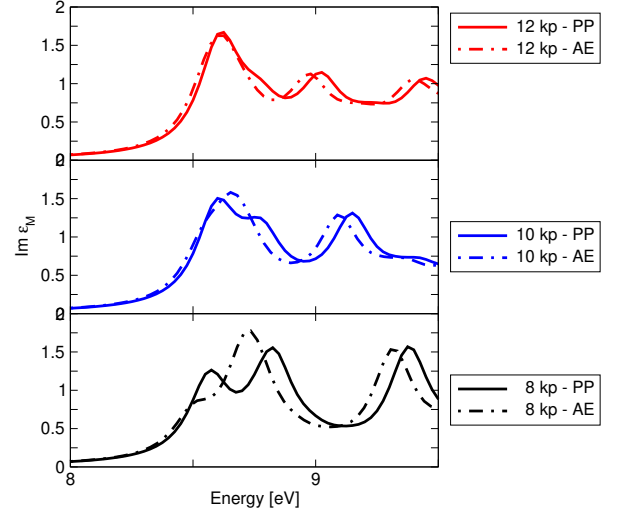


FIG. 5: Convergence of BSE absorption spectra calculated with pseudopotential (solid lines) and all-electron (dot-dashed lines) methods (with 2 conduction and 2 valence bands), for increasing number of \mathbf{k} points (Γ -centered grids with 8, 10 and 12 divisions for bottom, central and top panel, respectively).

entirely contained inside the MT^{85,112}. In order to overcome this problem, local orbitals are included to complement the basis. However, the quality of this basis set depends on the choice of energy parameters^{85,113}. In addition, there could be some interference effects that

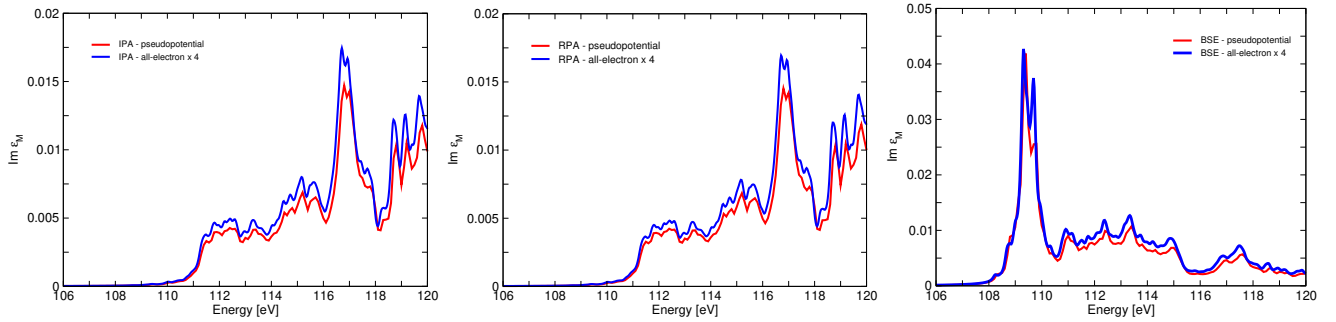


FIG. 6: Absorption spectra at the L_1 calculated with **EXC** (pseudopotential code) and **Exciting** (all-electron code). All the calculations are performed using a Γ -centered $8 \times 8 \times 8$ grid of \mathbf{k} points and 30 unoccupied bands. In **EXC** we include the 4 $2s$ levels corresponding to the 4 Al atoms, while in **Exciting** we include only one $2s$ level (i.e., the $2s$ state on the Al atom where the core hole is created). For this reason, the spectra of **Exciting** are multiplied $\times 4$.

play an important role, and are not obviously included when considering the states inside the muffin-tin⁸⁰. For all these reasons, since we validated the pseudopotential approach for the valence electrons (optical and L_{23} edge), we will use it to benchmark the L_1 edge.

The absorption spectra calculated for the L_1 edge using different levels of approximations are shown in Fig. 6. Notice that in **EXC**, the 4 bands corresponding to the $2s$ state of the 4 Al atoms need to be considered in order to properly represent the electronic transitions, while in **Exciting**, only one occupied level is considered, the $2s$ state of the Al atom where the core-hole is sitting. Since there are 4 equivalent Al atoms in the cell, the overall spectrum coming out of **Exciting** needs to be multiplied by 4, for a correct comparison.

In all level of approximations, the pseudopotential and all-electron results differ slightly (and more than in the optical or $L_{2,3}$ edge cases), showing that small interference effects among the Al atoms come to play. These interferences are small in the system under study, for the Al atoms lie in equivalent positions in the cell, but they are detectable. We have verified that in other systems⁸⁰ these effects can be quantitative and qualitatively more important. While including these effects is still feasible with **Exciting** (and all approaches that create a core-hole in a specific position), by doing multiple calculations and generalizing Eq. (2), interferences come up naturally in pseudopotential approaches, for all electrons are treated on the same footing and belong to the whole system, not just to one atom.

D. Optical and XANES spectra: valence and shallow core excitations

1. Comparison with experiments

Fig. 7 compares the calculated absorption spectra, $\text{Im}\epsilon_M(\omega)$, with experiment, for both the optical absorption corresponding to valence excitations and the XANES spectrum of the shallow-core excitations at the Al $L_{2,3}$

edge. The same figure also displays the results of the calculations at the Al L_1 edge, where, to best of our knowledge, no experimental XANES spectra are available for $\alpha\text{-Al}_2\text{O}_3$, since this core level excitation is less commonly studied than the Al K edge^{57,58,117,118}. In all cases, the presence of sharp and pronounced peaks at the onset of the BSE spectra (red lines), which are absent in the RPA and IPA spectra (orange and green lines), is an evidence of strong excitonic effects. Taking into account the electron-hole attraction in the BSE is the key to bring the calculations in agreement with experiment.

As already discussed in Ref. 93, for the optical absorption in the polarization direction perpendicular to the z axis (i.e. in the xy plane), where two VUV spectroscopy experiments^{114,115} are available, there are large discrepancies between the experimental spectra themselves [see Fig. 7(a)]. They agree on the position of the absorption onset and the presence of a sharp peak at ~ 9.2 eV, while they largely differ in the intensities of the various spectral features. Those differences can be attributed to the fact that both absorption spectra have been obtained from measured reflectivity data using the Kramers-Kronig relations, which introduces uncertainties in the $\text{Im}\epsilon_M(\omega)$ spectra. The calculated optical spectra in Fig. 7(a)-(b) have been blueshifted by 0.7 eV. This underestimation of the onset of the absorption spectrum is a manifestation of the underestimation of the band gap by the perturbative G_0W_0 approach, which is a systematic error for large gap materials¹¹⁹. As a matter of fact, the 2.64 eV scissor correction that we have employed here, which is taken from the G_0W_0 calculation in Ref. 93, underestimates the band gap correction to the LDA. The BSE calculation in Ref. 93 is also in very good agreement with the present result: the difference in the peak positions is actually due to the LDA band gap difference (see Sec. III A). The BSE spectrum in the xy polarization reproduces well the spectral shape measured by French *et al.*¹¹⁵, while there are larger differences with the experimental spectra in both polarizations measured by Tomiki *et al.*¹¹⁴.

At the Al $L_{2,3}$ edge, see Fig. 7(c), the calculated spec-

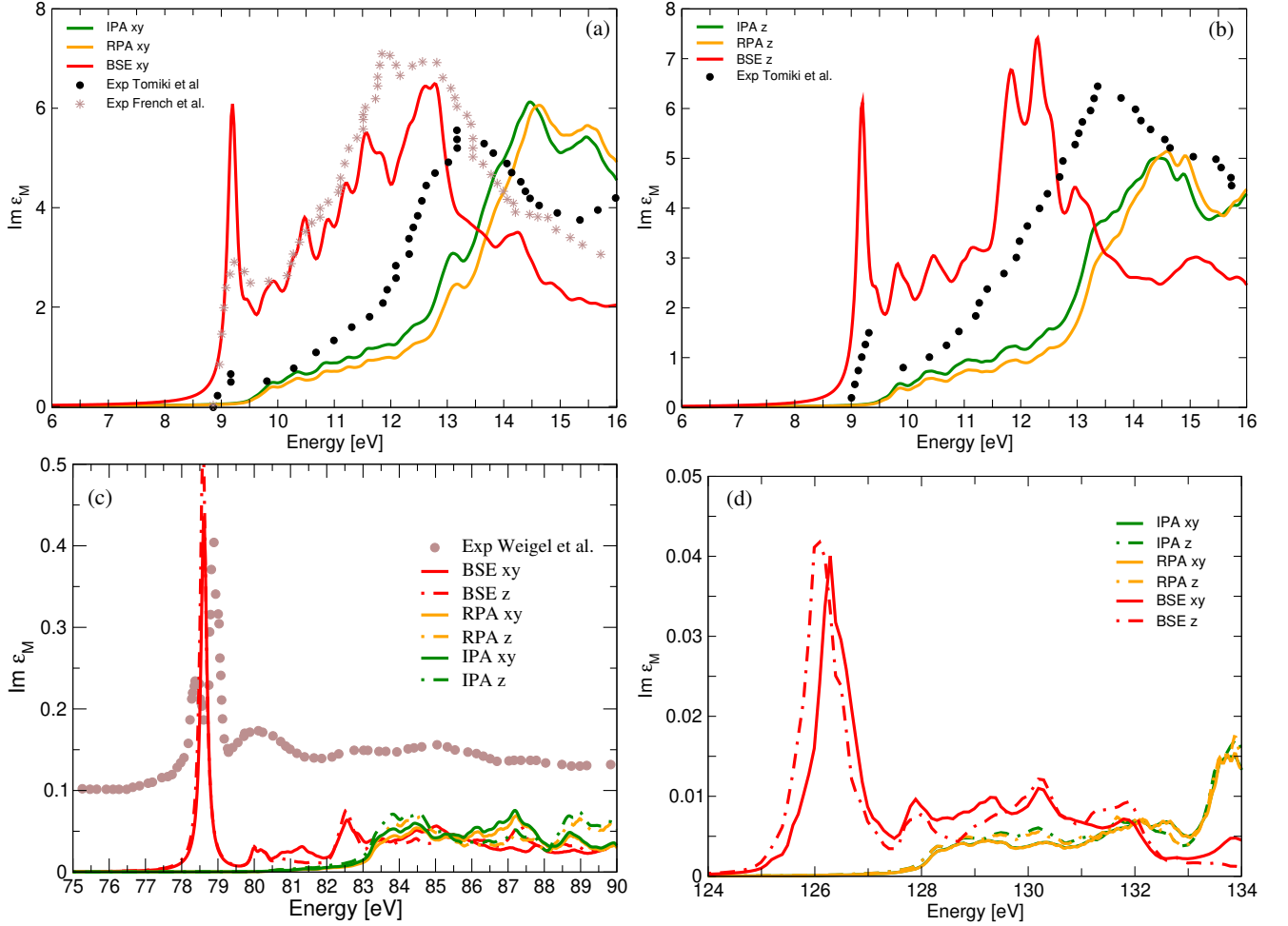


FIG. 7: Comparison of theoretical results with experimental data from Tomiki *et al.*¹¹⁴ and French *et al.*¹¹⁵ for the optical absorption, and Weigel *et al.*¹¹⁶ for the XANES at the $L_{2,3}$ edge. The calculated spectra are obtained in the independent particle approximation (IPA), green lines, in the random-phase approximation (RPA), orange lines, and from the solution of the Bethe-Salpeter equation (BSE), red lines. Optical absorption spectra for polarization in the (a) xy plane and (b) in the z direction: the calculated spectra have been blueshifted by 0.7 eV. (c) Absorption spectra at the $L_{2,3}$ edge in the xy (solid lines) and z (dot-dashed lines) polarizations compared to the isotropic XANES experimental spectrum¹¹⁶, to which a vertical offset has been added for improved clarity. (d) Absorption spectra at the L_1 edge in the xy (solid lines) and z (dot-dashed lines) polarizations.

tra have been blueshifted by 9.75 eV, which matches well the needed correction to the LDA Al $2p$ core level energy (see Sec. III A). The calculations neglect the spin-orbit coupling and therefore miss the splitting of the main peak into a doublet separated by 0.47 eV in the high-resolution experimental XANES spectrum from Ref. 116 (which also agrees well with previous experiments^{114,120,121}). In the spectra, the first, most prominent, excitonic peak is followed by a series of lower intensity peaks. While the absolute intensity of the experimental spectrum¹¹⁶ is arbitrary, the relative intensity of the first and second peaks gives information about the coordination number of Al and the nature of the chemical bond: a lower symmetry enhances the intensity of the second peak. Moreover, a lower coordination shifts the edge to lower energies, while higher bond ionicity shifts the edge to higher

energies^{59,116}.

At the Al L_1 edge there is no available experiment. Therefore, the curves in Fig. 7(d) have been shifted by 19.5 eV, in order for the smallest independent-particle transition energy, from the $2s$ band to the bottom-conduction band, to match the experimental value of 125.2 eV, which corresponds to the sum of the fundamental band gap plus the binding energy of the $2s$ states^{55,100} (see Sec. III A). We find that the main prominent excitonic peak in the BSE spectra is preceded by a pre-edge structure, more evident in the xy direction (solid lines). At the Al K edge, which mainly probes the analogous $1s \rightarrow 3p$ transition, there has been much work to explain the origin of a similar prepeak structure^{12,57,122–127}, which has been finally interpreted in terms of atomic vibrations enabling monopole transitions to unoccupied Al

3s states. In the present case, the calculations do not take into account the coupling with atomic vibrations and nevertheless the BSE spectra show a prepeak structure. This finding therefore calls for a detailed comparison with other calculations including atomic vibrations and, possibly, experiments at the Al L_1 edge.

2. Anisotropy and local field effects

The α -Al₂O₃ crystal is optically uniaxial. As shown by Fig. 7(a)-(b), at the onset of the optical spectrum the anisotropy is rather small, while it becomes larger for higher energy features. The lowest energy exciton is visible along the z polarization, while it is dark in the perpendicular xy polarization. It is separated by ~ 25 meV from a pair of degenerate excitons that are visible in the perpendicular xy direction and, conversely, dark in the z direction. Tomiki *et al.*¹¹⁴ experimentally determined a similar splitting of the exciton peaks in the two polarization directions (35 meV at room temperature and 86 meV at 10 K). We find that the binding energy of these excitons is of order of 0.3 eV, which is more than twice the 0.13 eV value estimated from temperature-dependent VUV spectroscopy⁵⁵. A similar splitting of the lowest energy exciton occurs also at the $L_{2,3}$ edge¹¹⁴, where its binding energy largely increases up to 1.6 eV. For the optical and the $L_{2,3}$ cases, both the lowest energy exciton in the BSE spectrum and the excitation at the smallest independent-particle transition energy in the IPA spectrum have a significant oscillator strength. Instead, at the L_1 edge the lowest energy transitions have a $2s \rightarrow 3s$ character and are dipole forbidden. We find that the binding energy of the lowest dark exciton at the L_1 edge is 1.2 eV. The lowest bright excitons in the z and xy polarization directions are located 1.6 eV and 1.8 eV above it, respectively. They belong to the prepeak in the spectrum. In this case, we define their binding energy as the difference with respect to the corresponding first allowed transition in the IPA spectrum: it amounts to 0.6 eV. The splitting of the main exciton peak in the two polarizations is also the largest one at the L_1 edge, being more than 0.2 eV.

By comparing the RPA and IPA optical spectra, orange and green lines in Fig. 7(a)-(b), respectively, we note that the effect of crystal local fields is quite small for both polarizations, in contrast to typical layered van der Waals materials like graphite, where local field effects are strong for the polarization along the hexagonal axis¹²⁸. Marinopoulos and Grüning⁹³ also found that local field effects are not essential to describe satisfactorily the low energy part of the experimental spectra, whereas they become crucial for higher energies (above 16 eV, not shown in Fig. 7), in correspondence to the excitation of the more localised O $2s$ electrons. Indeed, the degree of electron localisation directly correlates with the degree of charge inhomogeneity, which is a key factor for the induced microscopic local fields. One may therefore ex-

pect that the excitation spectra of shallow core levels, which are even more localised, should be more affected by local field effects. This phenomenon has been in fact observed for many shallow core levels^{129–133}. However, in α -Al₂O₃ for both the $L_{2,3}$ and L_1 edges the comparison of the absorption spectra calculated within the RPA and in the IPA shows that local field effects are actually negligible¹³⁴ (even weaker than in the optical regime). We can understand this result by noticing that the intensity of the $L_{2,3}$ and L_1 absorption spectra is one or two orders of magnitude smaller than for the optical absorption. This large intensity difference reflects the fact that Al $2p$ and $2s$ states are much less polarizable than valence states. Therefore, even though their electronic charge is much more localized and inhomogeneous, local fields associated to the excitations of Al $2p$ and $2s$ are small because they are weakly polarizable, which also leads to weak induced potentials.

3. Analysis of excitonic effects

Excitonic effects in solids can be understood as the result of the mixing of the independent-particle, vertical interband transitions at various \mathbf{k} points in the Brillouin zone, which are weighted by the excitonic coefficients $A_{v\mathbf{c}\mathbf{k}}^\lambda$, i.e., the eigenvectors of the excitonic Hamiltonian (1). The analysis of the excitonic coefficients therefore directly informs on the character of the exciton.

Fig. 8 represents, projected on the LDA band structure, the partial contributions $|A_{v\mathbf{c}\mathbf{k}}^\lambda \tilde{\rho}_{v\mathbf{c}\mathbf{k}}|$ to the oscillator strength of the lowest energy bright excitons in the absorption spectra of Fig. 7. Each independent-particle transition $v\mathbf{k} \rightarrow c\mathbf{k}$ is represented by a pair of circles, one in the occupied band v and one in the unoccupied band c , whose size is proportional to the value of the contribution. For the optical spectrum (left panel of Fig. 8), we consider the exciton giving rise to the first peak in the absorption spectrum in the z polarization. Our analysis shows that the largest contribution stems from the top-valence bottom-conduction transition at the Γ point, in correspondence to the direct band gap. The next \mathbf{k} points along the LFX line in the conduction band give a contribution that is already 10 times smaller. The others are even smaller. This is due to the fact that for this exciton the top-valence bottom-conduction transition at the Γ point has the predominant coefficient $A_{\lambda}^{v\mathbf{c}\mathbf{k}}$, together with a large single-particle oscillator strength $\tilde{\rho}_{v\mathbf{c}\mathbf{k}}$ in the z direction. Instead, the same $\tilde{\rho}_{v\mathbf{c}\mathbf{k}}$ is negligibly small in the x or y direction, explaining why the same exciton is dark in the xy plane.

For the $L_{2,3}$ and L_1 excitation spectra, all the \mathbf{k} points for the corresponding core levels are involved in the spectra, as one may expect from the fact that the core levels are not dispersive. Also for first exciton peak in the $L_{2,3}$ XANES spectrum (middle panel of Fig. 8), the lowest conduction band at the Γ point gives the largest contribution, having a large Al $3s$ character (see Sec. 3).

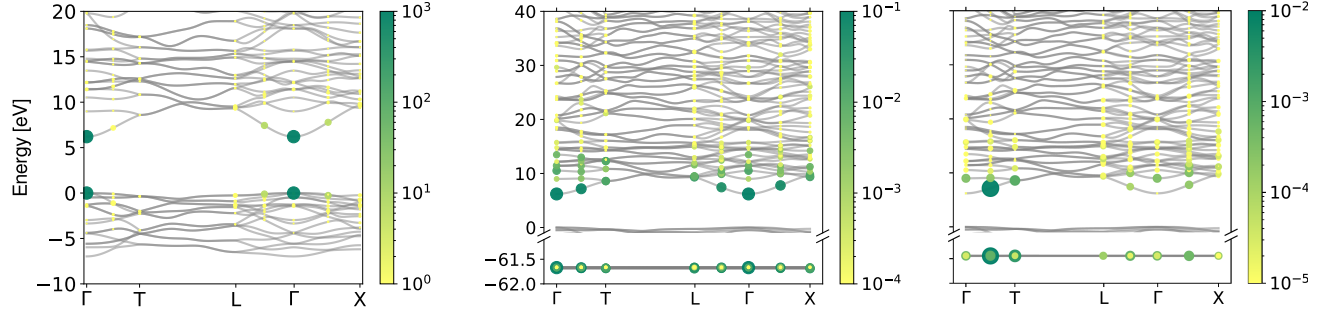


FIG. 8: Contributions of independent transitions to the lowest energy bright exciton intensity in the absorption spectra: (left) for the optical spectrum; (middle) for the XANES at $L_{2,3}$; (right) for the XANES at the L_1 edge. The size of the circles is proportional to $|\tilde{\rho}_{vck} A_{\lambda}^{vck}|$.

However, in this case the other \mathbf{k} points of the bottom conduction band and the higher conduction bands significantly contribute to the spectrum as well. This illustrates the deviation from a simple independent-particle picture of a $Al\ 2p \rightarrow 3s$ atomic transition, since many transitions are mixed together to produce the excitonic peak at the onset of the $L_{2,3}$ XANES spectrum.

For the L_1 XANES spectrum (right panel of Fig. 8), we consider the first bright exciton in the z polarization direction, which belongs to the prepeak in the spectrum in Fig. 7(d). Contrary to the other two cases, the bottom-conduction band at the Γ point gives no contribution, consistently with the $2s \rightarrow 3s$ character of the transition, which is dipole forbidden. The largest contributions are instead given by the \mathbf{k} points along the ΓT line of the bottom conduction band, which have $3p$ character as well. Even in this case higher conduction bands contribute significantly to the intensity of the excitonic prepeak.

The plot in Fig. 9 of the cumulative sums $S_{\lambda}(\omega)$, see Eq. (3), as a function of the number of conduction bands explains the different convergence behavior between the optical and $L_{2,3}$ XANES spectra shown in Fig. 1. By increasing the number of conduction bands in the BSE Hamiltonian (1), the largest possible independent-particle transition energy progressively increases. Therefore, the curves for larger numbers of conduction bands extend to higher energies. However, in the case of the optical spectrum (top panel), the cumulative sum $S_{\lambda}(\omega)$ rapidly converges to the final result. Already considering transition energies within 12 eV from the smallest one and including 15 conduction bands in the BSE hamiltonian give a result of the oscillator strength very close to 100%. Instead, in the case of the $L_{2,3}$ edge (bottom panel), the range of transition energies needed to get close to 100% has to be much larger, of the order of 50 eV above the smallest transition energy. Moreover, the various curves in the bottom panel of Fig. 9 do not overlap, as it is the case for the optical spectrum in the upper panel. This behavior indicates that, at the $L_{2,3}$ edge, interband transitions to higher conduction bands in the BSE hamiltonian mix together with transitions to lower

conduction bands, which affects the behavior of the cumulative sum $S_{\lambda}(\omega)$ also at lower energies. The reason of this strong mixing is the fact that at the $L_{2,3}$ edge there are many interband transitions with similar weak intensity. This, in turns, explains why the convergence of the XANES spectrum with the number of conduction bands is slow (see Fig. 1), and requires extra care.

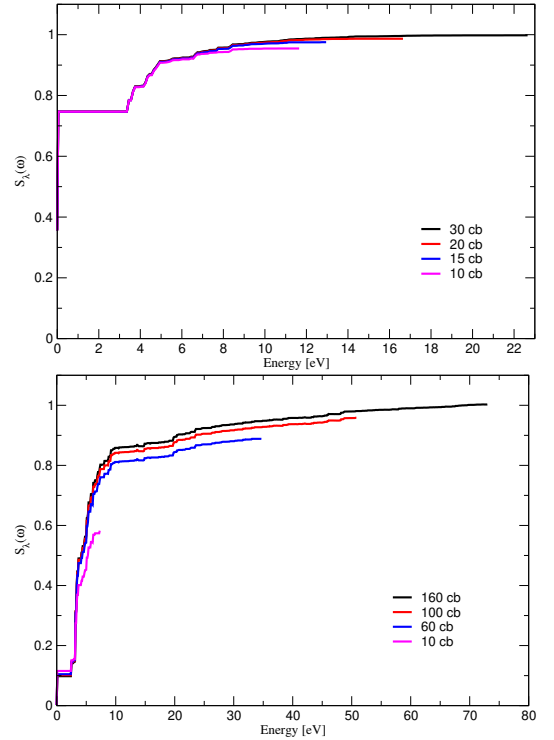


FIG. 9: Cumulative sums $S_{\lambda}(\omega)$ as a function of number of conduction bands (cb) in the BSE hamiltonian for the lowest energy bright exciton in the z direction for (top panel) the optical spectrum (bottom panel) and the XANES spectrum at the $L_{2,3}$ edge. In each case, the zero of the energy axis has been set to the smallest independent-particle transition energy and $S_{\lambda}(\omega)$ has been normalised to its largest value.

The lowest-energy dark excitons, both in the optical spectrum and the $L_{2,3}$ edge, have a cumulative sum $S_\lambda(\omega)$ that is always close to zero. It means that all the independent-particle oscillator strengths $\tilde{\rho}_{vck}$ are always small, indicating dipole forbidden transitions. The situation is instead different for the lowest dark exciton at the L_1 edge. In this case, some transitions to the lowest conduction bands have a weak but not zero contribution $|\tilde{\rho}_{vck}A_\lambda|$ to the spectrum, as shown by their representation on the LDA band structure in the top panel of Fig. 10. The corresponding cumulative sum $S_\lambda(\omega)$, bottom panel of Fig. 10, is indeed not always zero: it has even two distinct peaks, before progressively decreasing to zero, giving rise to a dark exciton. This suggests the occurrence of destructive interference of contributions $\tilde{\rho}_{vck}A_\lambda$ of different sign, involving transitions over a large range of energy. Moreover, it also shows that including not enough conduction bands in the BSE hamiltonian (1) would produce a weak excitonic peak in the spectrum. It is another indication that an independent-particle picture is here inadequate, whereas the strong electron-hole interaction manifest itself as the (positive or negative) interference of many electron-hole pairs.

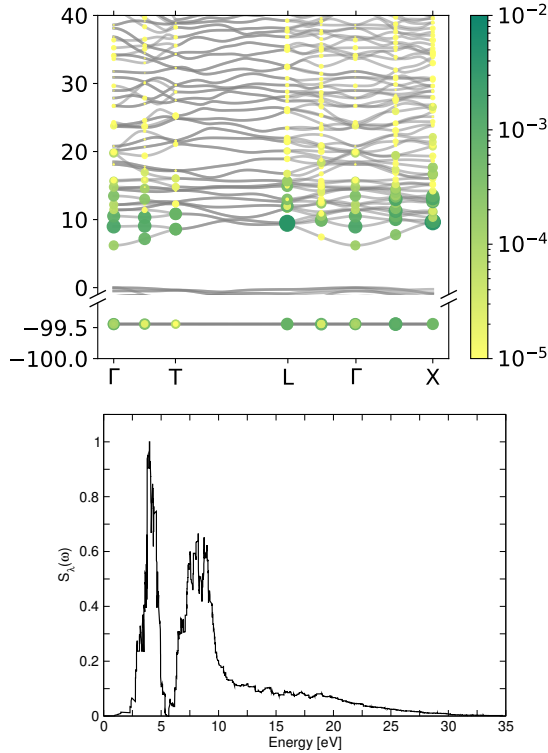


FIG. 10: Contributions of independent transitions to the dipole strength of the lowest energy dark exciton in the XANES spectrum at the L_1 edge. (Top panel) The size of the circle is proportional to $|\tilde{\rho}_{vck}A_\lambda|$. (Bottom panel) Corresponding cumulative sum $S_\lambda(\omega)$. The zero of the energy axis has been set to the smallest independent-particle transition energy and the intensity normalised to the largest value.

Fig. 11 displays the electron density distribution $|\Psi_\lambda(\mathbf{r}_h^0, \mathbf{r}_e)|^2$ for a fixed position of the hole \mathbf{r}_h^0 for the wavefunction of the lowest bright excitons in the spectra. In the color plots, we consider a cut of the three-dimensional distribution in the xy plane, perpendicular to the z axis, containing the hole. In all cases, the hole position (represented by the black ball in Fig. 11) has been chosen slightly away from the atoms, in order to avoid the nodes of the orbitals. This is the reason why the electron distribution is not symmetrical around the hole. For an uncorrelated electron-hole pair, the electron density would be delocalised all over the crystal, corresponding to a Bloch wavefunction. The effect of the electron-hole correlation is instead to localise the electron density around the hole.

For the optical spectrum (left panel), the hole has been placed near an O atom, consistently with the main character of the valence band (see Sec. III A). Here we discover that the electron charge is also surprisingly located at the O atoms, and quite delocalised in the xy plane. This picture is indeed in contrast with the naive expectation of a charge transfer O \rightarrow Al nature of the exciton, which is based on the largely ionic character of the electronic properties of α - Al_2O_3 . However, the strong Al-O hybridisation of the bottom conduction bands makes it possible for the exciton to localise entirely on the O atoms. The nature of the exciton in α - Al_2O_3 therefore turns out to be similar to what found^{135,136} in other ionic materials like LiF, where, analogously, for a hole fixed at a F atom, the electron charge is located mainly on F atoms as well.

Finally, the right panel of Fig. 11 shows the wavefunction of the first bright exciton in the prepeak of the L_1 edge. The hole is localised close to an Al atom. The resulting electron charge has partially the shape of a deformed $2p$ orbital pointing to the next neighbor O atom. In this case, the electron charge is entirely localised around the same Al site, displaying the atomic character of the core exciton.

IV. CONCLUSIONS

In summary, we have presented a norm-conserving pseudopotential approach that permits one to evaluate optical and XANES spectra on the same footing, using the same basis set for valence and shallow-core electrons. We have validated the approach by comparison with full potential all-electron calculations, at three different levels of theory, independent-particle approximation, RPA and full excitonic calculation, within the BSE formalism. We have applied this approach to study the optical and semi-core excitations of corundum α - Al_2O_3 , a promising material for its optical and structural properties. Both regimes, optical and XANES, present strong many-body effects that require the highest level of theory for an accurate and quantitative description. The BSE calculations show good agreement with experiments, when available,

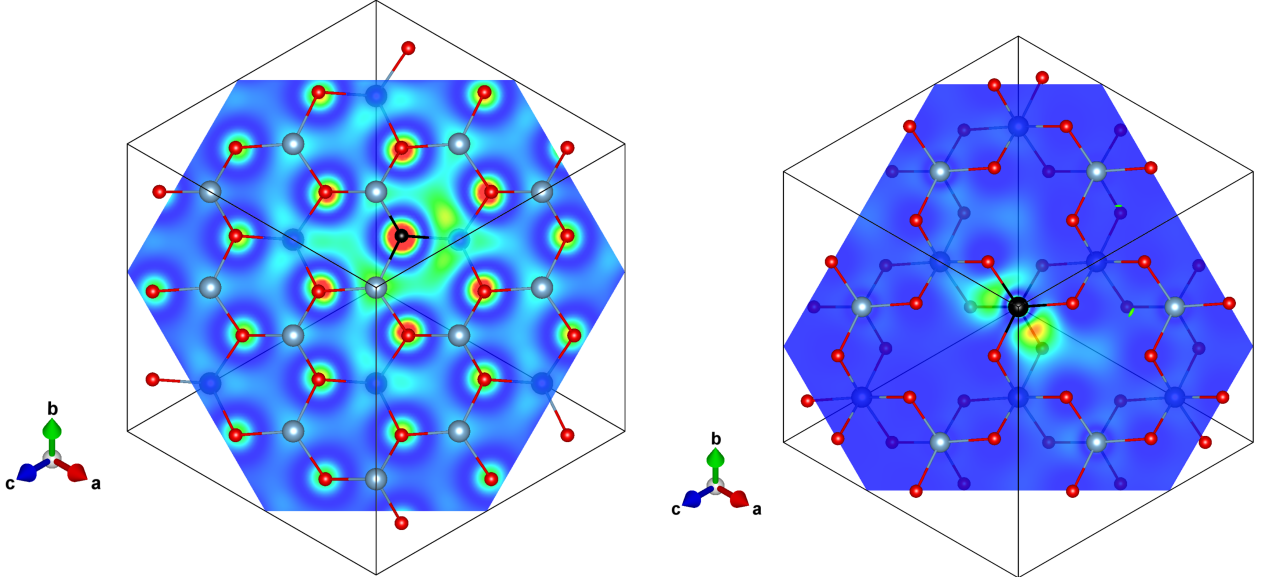


FIG. 11: Exciton correlation function $\Psi_\lambda(\mathbf{r}_h, \mathbf{r}_e)$ for the lowest bright exciton in the optical spectrum and at the prepeak at the L_1 edge. The position of the hole \mathbf{r}_h is fixed at \mathbf{r}_h^0 (see black ball). The color plots show the corresponding electron density distribution $|\Psi_\lambda(\mathbf{r}_h^0, \mathbf{r}_e)|^2$ in the xy plane perpendicular to the z axis containing the hole. In order to avoid nodes of the orbitals, the hole position has been slightly displaced from an oxygen atom for the optical exciton, and from an aluminum atom for the L_1 edge. (This explains why the density distributions are not symmetric around \mathbf{r}_h^0). The intensity follows a blue-cyan-green-yellow-orange-red gradient, and goes from 0 (blue) to the maximum value of the square of the excitonic wavefunctions (red).

but more importantly permit one to explain the physical origin of the various excitations, thanks to a thorough analysis of the excitons. The small anisotropy in the optical regime, for instance, reveals a different order of excitons in the z and perpendicular xy directions: the first exciton in bright along z , followed by dark excitons, while it is the contrary in the perpendicular xy direction. This splitting appears also for the $L_{2,3}$ edge. The dark/bright character of the excitons in the optical, L_1 and $L_{2,3}$ edges is analysed both by projecting the excitonic eigenvectors on the LDA band structure, as well as by looking at the cumulative function, Eq. (3). The first analysis tool is particularly useful to understand the origin of each exciton, in terms of the single-particle transitions and of the atomic characters of the single bands; the cumulative function can reveal purely many-body effects, like the destructive interference that takes place at the L_1 edge, making the first exciton dark. In addition, the excitonic wavefunction, by showing the localization of the

different excitons, can reveal counter-intuitive behaviour, like the electron localization on the oxygen atom, for the bright exciton in the optical spectrum, in contrast to a naive charge-transfer $O \rightarrow Al$ character.

This work opens the way to the treatment of other shallow-core spectroscopies, like electron energy loss near-edge structures (ELNES). Moreover, the unified footing to tackle shallow core, valence, and conduction states, will be particularly useful to describe Resonant Inelastic X-ray Scattering (RIXS) and X-ray Raman Scattering (XRS).

ACKNOWLEDGMENTS

We thank the French Agence Nationale de la Recherche (ANR) for financial support (Grant Agreements No. ANR-19-CE30-0011). Computational time was granted by GENCI (Project No. 544).

¹ J. van Bokhoven and C. Lamberti, eds., *X-Ray Absorption and X-Ray Emission Spectroscopy: Theory and Applications* (Wiley, 2016).

² F. M. de Groot, H. Elnaggar, F. Frati, R. pan Wang, M. U. Delgado-Jaime, M. van Veenendaal, J. Fernandez-Rodriguez, M. W. Haverkort, R. J. Green, G. van der Laan, Y. Kvashnin, A. Hariki, H. Ikeno, H. Ramanan-

toanina, C. Daul, B. Delley, M. Odelius, M. Lundberg, O. Kuhn, S. I. Bokarev, E. Shirley, J. Vinson, K. Gilmore, M. Stener, G. Fronzoni, P. Decleva, P. Kruger, M. Retegan, Y. Joly, C. Vorwerk, C. Draxl, J. Rehr, and A. Tanaka, *Journal of Electron Spectroscopy and Related Phenomena* **249**, 147061 (2021).

³ T. Fujikawa, *Journal of the Physical Society of Japan* **52**,

- 4001 (1983).
- ⁴ T. A. Tyson, K. O. Hodgson, C. R. Natoli, and M. Benfatto, *Phys. Rev. B* **46**, 5997 (1992).
 - ⁵ D. Ahlers, G. Schütz, V. Popescu, and H. Ebert, *Journal of Applied Physics* **83**, 7082 (1998).
 - ⁶ J. J. Rehr and R. C. Albers, *Rev. Mod. Phys.* **72**, 621 (2000).
 - ⁷ J. J. Rehr, J. J. Kas, M. P. Prange, A. P. Sorini, Y. Takimoto, and F. Vila, *Comptes Rendus Physique* **10**, 548 (2009).
 - ⁸ J. J. Rehr, J. J. Kas, F. D. Vila, M. P. Prange, and K. Jorissen, *Phys. Chem. Chem. Phys.* **12**, 5503 (2010).
 - ⁹ F. de Groot, *Coordination Chemistry Reviews* **249**, 31 (2005), synchrotron Radiation in Inorganic and Bioinorganic Chemistry.
 - ¹⁰ F. De Groot and A. Kotani, *Core level spectroscopy of solids* (CRC press, 2008).
 - ¹¹ M. W. Haverkort, M. Zwierzycki, and O. K. Andersen, *Phys. Rev. B* **85**, 165113 (2012).
 - ¹² S.-D. Mo and W. Y. Ching, *Phys. Rev. B* **62**, 7901 (2000).
 - ¹³ C. Gougoussis, M. Calandra, A. P. Seitsonen, and F. Mauri, *Phys. Rev. B* **80**, 075102 (2009).
 - ¹⁴ M. Taillefumier, D. Cabaret, A.-M. Flank, and F. Mauri, *Phys. Rev. B* **66**, 195107 (2002).
 - ¹⁵ O. Bunău and M. Calandra, *Phys. Rev. B* **87**, 205105 (2013).
 - ¹⁶ S. Mazevet, M. Torrent, V. Recoules, and F. Jollet, *High Energy Density Physics* **6**, 84 (2010).
 - ¹⁷ B. Hetényi, F. De Angelis, P. Giannozzi, and R. Car, *The Journal of Chemical Physics* **120**, 8632 (2004).
 - ¹⁸ D. Prendergast and G. Galli, *Phys. Rev. Lett.* **96**, 215502 (2006).
 - ¹⁹ S.-P. Gao, C. J. Pickard, A. Perlov, and V. Milman, *Journal of Physics: Condensed Matter* **21**, 104203 (2009).
 - ²⁰ J. C. A. Prentice, J. Aarons, J. C. Womack, A. E. A. Allen, L. Andrinopoulos, L. Anton, R. A. Bell, A. Bhandari, G. A. Bramley, R. J. Charlton, R. J. Clements, D. J. Cole, G. Constantinescu, F. Corsetti, S. M.-M. Dubois, K. K. B. Duff, J. M. Escartín, A. Greco, Q. Hill, L. P. Lee, E. Linscott, D. D. O'Regan, M. J. S. Phipps, L. E. Ratcliff, A. R. Serrano, E. W. Tait, G. Teobaldi, V. Vitale, N. Yeung, T. J. Zuehlsdorff, J. Dziedzic, P. D. Haynes, N. D. M. Hine, A. A. Mostofi, M. C. Payne, and C.-K. Skylaris, *The Journal of Chemical Physics* **152**, 174111 (2020), <https://doi.org/10.1063/5.0004445>.
 - ²¹ H. P. Hjalmarson, H. Büttner, and J. D. Dow, *Phys. Rev. B* **24**, 6010 (1981).
 - ²² K. Lie, R. Brydson, and H. Davock, *Phys. Rev. B* **59**, 5361 (1999).
 - ²³ L. Triguero, L. G. M. Pettersson, and H. Ågren, *Phys. Rev. B* **58**, 8097 (1998).
 - ²⁴ B. P. Klein, S. J. Hall, and R. J. Maurer, *Journal of Physics: Condensed Matter* **33**, 154005 (2021).
 - ²⁵ J. J. Rehr, J. A. Soininen, and E. L. Shirley, *Physica Scripta* **2005**, 207 (2005).
 - ²⁶ Y. Liang, J. Vinson, S. Pemmaraju, W. S. Drisdell, E. L. Shirley, and D. Prendergast, *Phys. Rev. Lett.* **118**, 096402 (2017).
 - ²⁷ G. Onida, L. Reining, and A. Rubio, *Rev. Mod. Phys.* **74**, 601 (2002).
 - ²⁸ N. A. Besley, M. J. G. Peach, and D. J. Tozer, *Phys. Chem. Chem. Phys.* **11**, 10350 (2009).
 - ²⁹ O. Bunău and Y. Joly, *Phys. Rev. B* **85**, 155121 (2012).
 - ³⁰ O. Bunău and Y. Joly, *Journal of Physics: Condensed Matter* **24**, 215502 (2012).
 - ³¹ G. Strinati, *Phys. Rev. Lett.* **49**, 1519 (1982).
 - ³² G. Strinati, *Phys. Rev. B* **29**, 5718 (1984).
 - ³³ E. L. Shirley, *Phys. Rev. Lett.* **80**, 794 (1998).
 - ³⁴ J. A. Carlisle, E. L. Shirley, L. J. Terminello, J. J. Jia, T. A. Callcott, D. L. Ederer, R. C. C. Perera, and F. J. Himpsel, *Phys. Rev. B* **59**, 7433 (1999).
 - ³⁵ E. Shirley, *Journal of Physics and Chemistry of Solids* **61**, 445 (2000).
 - ³⁶ R. M. Martin, L. Reining, and D. M. Ceperley, *Interacting Electrons: Theory and Computational Approaches* (Cambridge University Press, 2016).
 - ³⁷ F. Bechstedt, *Many-Body Approach to Electronic Excitations: Concepts and Applications*, Springer Series in Solid-State Sciences (Springer Berlin Heidelberg, 2014).
 - ³⁸ S. Botti, A. Schindlmayr, R. D. Sole, and L. Reining, *Reports on Progress in Physics* **70**, 357 (2007).
 - ³⁹ J. Wills, M. Alouani, P. Andersson, A. Delin, O. Eriksson, and O. Grechnev, *Full-Potential Electronic Structure Method: Energy and Force Calculations with Density Functional and Dynamical Mean Field Theory*, Springer Series in Solid-State Sciences (Springer Berlin Heidelberg, 2010).
 - ⁴⁰ O. K. Andersen, *Phys. Rev. B* **12**, 3060 (1975).
 - ⁴¹ E. Sjöstedt, L. Nordström, and D. Singh, *Solid State Communications* **114**, 15 (2000).
 - ⁴² G. K. H. Madsen, P. Blaha, K. Schwarz, E. Sjöstedt, and L. Nordström, *Phys. Rev. B* **64**, 195134 (2001).
 - ⁴³ M. C. Payne, M. P. Teter, D. C. Allan, T. A. Arias, and J. D. Joannopoulos, *Rev. Mod. Phys.* **64**, 1045 (1992).
 - ⁴⁴ W. Ku and A. G. Eguluz, *Phys. Rev. Lett.* **89**, 126401 (2002).
 - ⁴⁵ K. Delaney, P. García-González, A. Rubio, P. Rinke, and R. W. Godby, *Phys. Rev. Lett.* **93**, 249701 (2004).
 - ⁴⁶ M. L. Tiago, S. Ismail-Beigi, and S. G. Louie, *Phys. Rev. B* **69**, 125212 (2004).
 - ⁴⁷ M. van Schilfgaarde, T. Kotani, and S. V. Faleev, *Phys. Rev. B* **74**, 245125 (2006).
 - ⁴⁸ C. Friedrich, A. Schindlmayr, S. Blügel, and T. Kotani, *Phys. Rev. B* **74**, 045104 (2006).
 - ⁴⁹ R. Gómez-Abal, X. Li, M. Scheffler, and C. Ambrosch-Draxl, *Phys. Rev. Lett.* **101**, 106404 (2008).
 - ⁵⁰ E. Luppi, H.-C. Weissker, S. Bottaro, F. Sottile, V. Veniard, L. Reining, and G. Onida, *Phys. Rev. B* **78**, 245124 (2008).
 - ⁵¹ J. c. v. Klimeš, M. Kaltak, and G. Kresse, *Phys. Rev. B* **90**, 075125 (2014).
 - ⁵² D. R. Hamann, *Phys. Rev. B* **88**, 085117 (2013).
 - ⁵³ The same hypothesis is made when the core orbitals are obtained from a calculation of the isolated atom^{81,137,138}.
 - ⁵⁴ R. H. French, *Journal of the American Ceramic Society* **73**, 477 (1990).
 - ⁵⁵ R. H. French, D. J. Jones, and S. Loughin, *Journal of the American Ceramic Society* **77**, 412 (1994).
 - ⁵⁶ I. Tanaka and H. Adachi, *Phys. Rev. B* **54**, 4604 (1996).
 - ⁵⁷ D. Cabaret, P. Saintavit, P. Ildefonse, and A.-M. Flank, *Journal of Physics: Condensed Matter* **8**, 3691 (1996).
 - ⁵⁸ P. Ildefonse, D. Cabaret, P. Saintavit, G. Calas, A.-M. Flank, and P. Lagarde, *Physics and Chemistry of Minerals* **25**, 112 (1998).
 - ⁵⁹ J. A. van Bokhoven, T. Nabi, H. Sambe, D. E. Ramaker, and D. C. Koningsberger, *Journal of Physics: Condensed Matter* **13**, 10247 (2001).
 - ⁶⁰ G. Strinati, *Rivista del Nuovo Cimento* **11**, 1 (1988).

- ⁶¹ L. Hedin, Phys. Rev. **139**, A796 (1965).
- ⁶² S. Albrecht, L. Reining, R. Del Sole, and G. Onida, Phys. Rev. Lett. **80**, 4510 (1998).
- ⁶³ L. X. Benedict, E. L. Shirley, and R. B. Bohn, Phys. Rev. Lett. **80**, 4514 (1998).
- ⁶⁴ M. Rohlfing and S. G. Louie, Phys. Rev. B **62**, 4927 (2000).
- ⁶⁵ J. Vinson, J. J. Rehr, J. J. Kas, and E. L. Shirley, Phys. Rev. B **83**, 115106 (2011).
- ⁶⁶ J. Vinson and J. J. Rehr, Phys. Rev. B **86**, 195135 (2012).
- ⁶⁷ K. Gilmore, J. Vinson, E. Shirley, D. Prendergast, C. Pemmaraju, J. Kas, F. Vila, and J. Rehr, Computer Physics Communications **197**, 109 (2015).
- ⁶⁸ K. Gilmore, J. Pellicciari, Y. Huang, J. J. Kas, M. Dantz, V. N. Strocov, S. Kasahara, Y. Matsuda, T. Das, T. Shibauchi, and T. Schmitt, Phys. Rev. X **11**, 031013 (2021).
- ⁶⁹ A. Geondzhian and K. Gilmore, Phys. Rev. B **98**, 214305 (2018).
- ⁷⁰ C. D. Dashwood, A. Geondzhian, J. G. Vale, A. C. Pakpour-Tabrizi, C. A. Howard, Q. Faure, L. S. I. Veiga, D. Meyers, S. G. Chiuzbaian, A. Nicolaou, N. Jaouen, R. B. Jackman, A. Nag, M. García-Fernández, K.-J. Zhou, A. C. Walters, K. Gilmore, D. F. McMorro, and M. P. M. Dean, Phys. Rev. X **11**, 041052 (2021).
- ⁷¹ J. Vinson, Phys. Chem. Chem. Phys. **24**, 12787 (2022).
- ⁷² W. Olovsson, I. Tanaka, P. Puschnig, and C. Ambrosch-Draxl, Journal of Physics: Condensed Matter **21**, 104205 (2009).
- ⁷³ W. Olovsson, I. Tanaka, T. Mizoguchi, P. Puschnig, and C. Ambrosch-Draxl, Phys. Rev. B **79**, 041102 (2009).
- ⁷⁴ W. Olovsson, I. Tanaka, T. Mizoguchi, G. Radtke, P. Puschnig, and C. Ambrosch-Draxl, Phys. Rev. B **83**, 195206 (2011).
- ⁷⁵ C. Vorwerk, C. Cocchi, and C. Draxl, Phys. Rev. B **95**, 155121 (2017).
- ⁷⁶ C. Vorwerk, B. Aurich, C. Cocchi, and C. Draxl, Electronic Structure **1**, 037001 (2019).
- ⁷⁷ C. Vorwerk, F. Sottile, and C. Draxl, Phys. Rev. Research **2**, 042003 (2020).
- ⁷⁸ R. Laskowski and P. Blaha, Phys. Rev. B **82**, 205104 (2010).
- ⁷⁹ Y. Yao, D. Golze, P. Rinke, V. Blum, and Y. Kanai, Journal of Chemical Theory and Computation **18**, 1569 (2022).
- ⁸⁰ C. Vorwerk, F. Sottile, and C. Draxl, Phys. Chem. Chem. Phys. **24**, 17439 (2022).
- ⁸¹ M. Unzog, A. Tal, and G. Kresse, Phys. Rev. B **106**, 155133 (2022).
- ⁸² There is also the possibility to include $-W$ and exclude \bar{v}_c , which corresponds to the description of spin-triplet excitations.
- ⁸³ X. Gonze, F. Jollet, F. Abreu Araujo, D. Adams, B. Amadon, T. Applencourt, C. Audouze, J.-M. Beuken, J. Bieder, A. Bokhanchuk, E. Bousquet, F. Bruneval, D. Caliste, M. Côté, F. Dahm, F. Da Pieve, M. Delaveau, M. Di Gennaro, B. Dorado, C. Espejo, G. Geneste, L. Genovese, A. Gerossier, M. Giantomassi, Y. Gillet, D. Hamann, L. He, G. Jomard, J. Laflamme Janssen, S. Le Roux, A. Levitt, A. Lherbier, F. Liu, I. Lukačević, A. Martin, C. Martins, M. Oliveira, S. Poncé, Y. Pouillon, T. Rangel, G.-M. Rignanese, A. Romero, B. Rousseau, O. Rubel, A. Shukri, M. Stankovski, M. Torrent, M. Van Setten, B. Van Troeye, M. Verstraete, D. Waroquiers, J. Wiktor, B. Xu, A. Zhou, and J. Zwanziger, Comput. Phys. Commun. **205**, 106 (2016).
- ⁸⁴ L. Reining, V. Olevano, F. Sottile, S. Albrecht, and G. Onida, “The exc code,” https://etsf.polytechnique.fr/software/Ab_Initio/, unpublished.
- ⁸⁵ A. Gulans, S. Kontur, C. Meisenbichler, D. Nabok, P. Pavone, S. Rigamonti, S. Sagmeister, U. Werner, and C. Draxl, Journal of Physics: Condensed Matter **26**, 363202 (2014).
- ⁸⁶ W. Kohn and L. J. Sham, Phys. Rev. **140**, A1133 (1965).
- ⁸⁷ N. Troullier and J. L. Martins, Phys. Rev. B **43**, 1993 (1991).
- ⁸⁸ M. van Setten, M. Giantomassi, E. Bousquet, M. Verstraete, D. Hamann, X. Gonze, and G.-M. Rignanese, Computer Physics Communications **226**, 39 (2018).
- ⁸⁹ J. S. Zhou, L. Reining, A. Nicolaou, A. Bendounan, K. Ruotsalainen, M. Vanzini, J. J. Kas, J. J. Rehr, M. Muntwiler, V. N. Strocov, F. Sirotti, and M. Gatti, Proceedings of the National Academy of Sciences **117**, 28596 (2020).
- ⁹⁰ K. Sturm, E. Zaremba, and K. Nuroh, Phys. Rev. B **42**, 6973 (1990).
- ⁹¹ A. A. Quong and A. G. Eguiluz, Phys. Rev. Lett. **70**, 3955 (1993).
- ⁹² J. S. Zhou, M. Gatti, J. J. Kas, J. J. Rehr, and L. Reining, Phys. Rev. B **97**, 035137 (2018).
- ⁹³ A. G. Marinopoulos and M. Grüning, Phys. Rev. B **83**, 195129 (2011).
- ⁹⁴ A. Lorin, M. Gatti, L. Reining, and F. Sottile, Phys. Rev. B **104**, 235149 (2021).
- ⁹⁵ E. E. Newnham and Y. M. Haan, Zeitschrift für Kristallographie - Crystalline Materials **117**, 235 (1962).
- ⁹⁶ W. C. Mackrodt, M. Rérat, F. S. Gentile, and R. Dovesi, Journal of Physics: Condensed Matter **32**, 085901 (2019).
- ⁹⁷ R. Ahuja, J. M. Osorio-Guillen, J. S. de Almeida, B. Holm, W. Y. Ching, and B. Johansson, Journal of Physics: Condensed Matter **16**, 2891 (2004).
- ⁹⁸ R. Santos, E. Longhinotti, V. Freire, R. Reimberg, and E. Caetano, Chemical Physics Letters **637**, 172 (2015).
- ⁹⁹ F. G. Will, H. G. DeLorenzi, and K. H. Janora, Journal of the American Ceramic Society **75**, 295 (1992).
- ¹⁰⁰ B. Crist, *Handbooks of Monochromatic XPS Spectra: Volume 2 : Commercially Pure Binary Oxides* (XPS International LLC, 2004).
- ¹⁰¹ A. Willand, Y. O. Kvashnin, L. Genovese, A. Vázquez-Mayagoitia, A. K. Deb, A. Sadeghi, T. Deutsch, and S. Goedecker, The Journal of Chemical Physics **138**, 104109 (2013).
- ¹⁰² K. Lejaeghere, V. V. Speybroeck, G. V. Oost, and S. Cottenier, Critical Reviews in Solid State and Materials Sciences **39**, 1 (2014).
- ¹⁰³ G. Prandini, A. Marrazzo, I. E. Castelli, N. Mounet, and N. Marzari, npj Computational Materials **4**, 2057 (2018).
- ¹⁰⁴ K. Lejaeghere, G. Bihlmayer, T. Björkman, P. Blaha, S. Blügel, V. Blum, D. Caliste, I. E. Castelli, S. J. Clark, A. D. Corso, S. de Gironcoli, T. Deutsch, J. K. Dewhurst, I. D. Marco, C. Draxl, M. Dułak, O. Eriksson, J. A. Flores-Livas, K. F. Garrity, L. Genovese, P. Giannozzi, M. Giantomassi, S. Goedecker, X. Gonze, O. Grånäs, E. K. U. Gross, A. Gulans, F. Gygi, D. R. Hamann, P. J. Hasnip, N. A. W. Holzwarth, D. Iuşan, D. B. Jochym, F. Jollet, D. Jones, G. Kresse, K. Koepnick, E. Küçükbenli, Y. O. Kvashnin, I. L. M.

- Locht, S. Lubeck, M. Marsman, N. Marzari, U. Nitzsche, L. Nordström, T. Ozaki, L. Paulatto, C. J. Pickard, W. Poelmans, M. I. J. Probert, K. Refson, M. Richter, G.-M. Rignanese, S. Saha, M. Scheffler, M. Schlipf, K. Schwarz, S. Sharma, F. Tavazza, P. Thunström, A. Tkatchenko, M. Torrent, D. Vanderbilt, M. J. van Setten, V. V. Speybroeck, J. M. Wills, J. R. Yates, G.-X. Zhang, and S. Cottenier, *Science* **351**, aad3000 (2016), <https://www.science.org/doi/pdf/10.1126/science.aad3000>.
- ¹⁰⁵ X. Gonze, R. Stumpf, and M. Scheffler, *Phys. Rev. B* **44**, 8503 (1991).
- ¹⁰⁶ P. Puschnig and C. Ambrosch-Draxl, *Phys. Rev. B* **66**, 165105 (2002).
- ¹⁰⁷ T. Rangel, M. D. Ben, D. Varsano, G. Antonius, F. Bruneval, F. H. da Jornada, M. J. van Setten, O. K. Orhan, D. D. O'Regan, A. Canning, A. Ferretti, A. Marini, G.-M. Rignanese, J. Deslippe, S. G. Louie, and J. B. Neaton, *Computer Physics Communications* **255**, 107242 (2020).
- ¹⁰⁸ S. Albrecht, *Optical Absorption Spectra of Semiconductors and Insulators: ab initio calculations of many-body effects*, Ph.D. thesis, Ecole Polytechnique, Palaiseau (1999).
- ¹⁰⁹ P. Puschnig, *Excitonic Effects in Organic Semiconductors - An Ab-initio Study within the LAPW Method*, Ph.D. thesis (2002).
- ¹¹⁰ C. Freysoldt, P. Eggert, P. Rinke, A. Schindlmayr, and M. Scheffler, *Phys. Rev. B* **77**, 235428 (2008).
- ¹¹¹ F. Fuchs, C. Rödl, A. Schleife, and F. Bechstedt, *Phys. Rev. B* **78**, 085103 (2008).
- ¹¹² S. Goedecker, *Phys. Rev. B* **47**, 9881 (1993).
- ¹¹³ D. Singh, *Phys. Rev. B* **43**, 6388 (1991).
- ¹¹⁴ T. Tomiki, Y. Ganaha, T. Shikenbaru, T. Futeemma, M. Yuri, Y. Aiura, S. Sato, H. Fukutani, H. Kato, T. Miyahara, A. Yonesu, and J. Tamashiro, *Journal of the Physical Society of Japan* **62**, 573 (1993).
- ¹¹⁵ R. H. French, H. Mülleijans, and D. J. Jones, *Journal of the American Ceramic Society* **81**, 2549 (1998).
- ¹¹⁶ C. Weigel, G. Calas, L. Cormier, L. Galois, and G. S. Henderson, *Journal of Physics: Condensed Matter* **20**, 135219 (2008).
- ¹¹⁷ J. A. van Bokhoven, H. Sambe, D. E. Ramaker, and D. C. Koningsberger, *The Journal of Physical Chemistry B* **103**, 7557 (1999).
- ¹¹⁸ T. Mizoguchi, I. Tanaka, S.-P. Gao, and C. J. Pickard, *Journal of Physics: Condensed Matter* **21**, 104204 (2009).
- ¹¹⁹ M. van Schilfgaarde, T. Kotani, and S. Faleev, *Phys. Rev. Lett.* **96**, 226402 (2006).
- ¹²⁰ W. L. O'Brien, J. Jia, Q.-Y. Dong, T. A. Callcott, J.-E. Rubensson, D. L. Mueller, and D. L. Ederer, *Phys. Rev. B* **44**, 1013 (1991).
- ¹²¹ W. L. O'Brien, J. Jia, Q.-Y. Dong, T. A. Callcott, D. R. Mueller, D. L. Ederer, and C.-C. Kao, *Phys. Rev. B* **47**, 15482 (1993).
- ¹²² D. Cabaret, E. Gaudry, M. TAILLEFUMIER, P. Sainctavit, and F. Mauri, *Physica Scripta* **2005**, 131 (2005).
- ¹²³ D. Cabaret and C. Brouder, *Journal of Physics: Conference Series* **190**, 012003 (2009).
- ¹²⁴ C. Brouder, D. Cabaret, A. Juhin, and P. Sainctavit, *Phys. Rev. B* **81**, 115125 (2010).
- ¹²⁵ D. Manuel, D. Cabaret, C. Brouder, P. Sainctavit, A. Bordage, and N. Trcera, *Phys. Rev. B* **85**, 224108 (2012).
- ¹²⁶ R. Nemausat, C. Brouder, C. Gervais, and D. Cabaret, *Journal of Physics: Conference Series* **712**, 012006 (2016).
- ¹²⁷ S. Delhommaye, G. Radtke, C. Brouder, S. P. Collins, S. Huotari, C. Sahle, M. Lazzeri, L. Paulatto, and D. Cabaret, *Phys. Rev. B* **104**, 024302 (2021).
- ¹²⁸ A. G. Marinopoulos, L. Reining, V. Olevano, A. Rubio, T. Pichler, X. Liu, M. Knupfer, and J. Fink, *Phys. Rev. Lett.* **89**, 076402 (2002).
- ¹²⁹ N. Vast, L. Reining, V. Olevano, P. Schattschneider, and B. Jouffrey, *Phys. Rev. Lett.* **88**, 037601 (2002).
- ¹³⁰ L. Dash, F. Bruneval, V. Trinité, N. Vast, and L. Reining, *Computational Materials Science* **38**, 482 (2007), selected papers from the International Conference on Computational Methods in Sciences and Engineering 2004.
- ¹³¹ S. Huotari, J. A. Soininen, G. Vankó, G. Monaco, and V. Olevano, *Phys. Rev. B* **82**, 064514 (2010).
- ¹³² P. Cudazzo, K. O. Ruotsalainen, C. J. Sahle, A. Al-Zein, H. Berger, E. Navarro-Moratalla, S. Huotari, M. Gatti, and A. Rubio, *Phys. Rev. B* **90**, 125125 (2014).
- ¹³³ K. Ruotsalainen, A. Nicolaou, C. J. Sahle, A. Efimenko, J. M. Ablett, J.-P. Rueff, D. Prabhakaran, and M. Gatti, *Phys. Rev. B* **103**, 235136 (2021).
- ¹³⁴ It is well known that local field effects, expressed as electron-hole exchange interaction in the BSE framework, are essential to get the correct branching ratios between L_2 and L_3 components, see e.g.^{66,67,139}. However, in the present case the neglect of spin-orbit coupling does not allow us to resolve the two components. For α - Al_2O_3 an electron-hole exchange energy of 0.3 eV has been estimated^{116,120}.
- ¹³⁵ M. Rohlfing and S. G. Louie, *Phys. Rev. Lett.* **81**, 2312 (1998).
- ¹³⁶ M. Gatti and F. Sottile, *Phys. Rev. B* **88**, 155113 (2013).
- ¹³⁷ E. L. Shirley, *Journal of Electron Spectroscopy and Related Phenomena* **136**, 77 (2004), progress in Core-Level Spectroscopy of Condensed Systems.
- ¹³⁸ P. E. Blöchl, *Phys. Rev. B* **50**, 17953 (1994).
- ¹³⁹ A. L. Ankudinov, Y. Takimoto, and J. J. Rehr, *Phys. Rev. B* **71**, 165110 (2005).